1 **Technical note: Rapid phase identification of apatite and zircon grains for geochronology**

2 **using X-ray micro-computed tomography**

3 Emily H. G. Cooperdock[1]*, Florian Hofmann[1,2]*, Ryley M. Collins[1], Anahi Carrera[1], Aya

4 Takase[3], and Aaron J. Celestian[4]

5 [1]University of Southern California, Department of Earth Sciences, 3651 Trousdale Parkway, Los

6 Angeles, CA 90089, USA

7 [2]University of Alaska Fairbanks, Geophysical Institute, 900 Yukon Dr, Fairbanks, AK 99775,

8 USA

9 [3]Rigaku Americas Corporation, 9009 New Trails Drive, The Woodlands, TX 77381, USA

10 [4]Mineral Sciences Department, Natural History Museum of Los Angeles County, 900 Exposition

11 Boulevard, Los Angeles, California 90007, USA

12 *Authors contributed equally to this work.

13 *Correspondence to*: cooperdo@usc.edu

Abstract

14

15   Apatite and zircon are among the best-studied and most widely used accessory minerals

16 for geochronology and thermochronology. Given that apatite and zircon are often present in the

17 same lithologies, distinguishing the two phases in crushed mineral separates is a common task

18 for geochronology, thermochronology, and petrochronology studies. Here we present a method

19 for efficient and accurate apatite and zircon mineral phase identification and verification using

20 X-ray micro-computed tomography (microCT) of grain mounts that provides additional 3-

21 dimensional grain size, shape, and inclusion suite information. In this study, we analyzed apatite

22 and zircon grains from Fish Canyon Tuff samples that underwent methylene iodide (MEI) and

23 lithium heteropolytungstate (LST) heavy liquids density separations. We validate the microCT

24 results using known standards and phase identification with Raman spectroscopy demonstrating

25 that apatite and zircon are distinguishable from each other and other common phases, e.g.,

26 titanite, based on microCT X-ray density. We present recommended microCT scanning protocols

27 after systematically testing the effects of different scanning parameters and sample positions.

28 This methodology can help to reduce time spent performing density separations with highly toxic

29 chemicals and visually inspecting grains under a light microscope, and the improved mineral

30 identification and characterization can make geochronologic data more robust.

31

1 Introduction

33   Apatite and zircon are mineral phases widely used for geochronology and

34 thermochronology using the U-Pb (e.g., Bowring and Schmitz, 2003), (U-Th)/He (e.g. Farley,

35 2002), and fission track (e.g. Tagami and O'Sullivan, 2005) methods. Particularly for (U-Th)/He,

36 correct identification of these phases (e.g. Guenthner et al., 2016), characterization of the crystal

37 shape (Farley et al., 1996), and the absence of mineral and fluid inclusions (e.g. Lippolt et al.,

38 1994; Vermeesch et al., 2007) are important factors in producing reliable, high-quality geo- and

39 thermochronologic data. The standard approach to selecting apatite and zircon grains for geo-

40 and thermochronology is to 1) crush and grind rock samples into their mineral constituents, 2)

41 perform magnetic and density separation which may include a Frantz isodynamic separator,

42 water table, and heavy liquids to filter for the mineral of choice, and then 3) pick individual

43 grains from these separates under a transmitted light microscope (e.g., Gautheron et al., 2021).

44   Different heavy liquid solutions used for density separation can either produce grain

45   fractions that have apatite and zircon mixed together or separated (e.g., Dumitru and Stockli,

46   1998; Koroznikova et al., 2008). The density of apatite ($Ca_5(PO_4)_3(F,OH,Cl)$) is 3.10-3.25 g/cm^3

47   and depends on the solid solution composition between fluorapatite, chlorapatite, and

48   hydroxylapatite (Hughes et al., 1989). Zircon ($ZrSiO_4$) can display densities between 3.9 and 4.7

49   g/cm^3, depending on the degree of metamictization (Holland and Gottfried, 1955). Although

50   density-separated apatite and zircon fractions make picking the correct mineral easier (Dumitru

51   and Stockli, 1998), the process often includes the use of toxic halogenated organic solutions,

52   such as bromoform ($CHBr_3$) and diiodomethane (CH_2I_2, methylene iodide, commonly

53   abbreviated as MEI, MI, or DIM; e.g. Hauff and Airey, 1980). Typically, bromoform (2.89

54   g/cm^3) is used in a first step to separate quartz and feldspar and the resulting heavy fraction is

55   then treated with MEI (3.32 g/cm^3) to separate apatite and zircon (e.g. Dumitru and Stockli,

56   1998).

57   Both Bromoform and MEI are known to be toxic. Specifically, MEI can cause acute

58   symptoms through skin contact or inhalation, and acute toxicity and death have been documented

59   for a case of ingestion (Weimerskirch et al., 1990). MEI has also been shown to be mutagenic

60   meaning acute or long-term exposure may impact reproductive health, particularly in pregnant

61   women (Van Bladeren et al., 1980; Osterman-Golkar et al., 1983; Buijs et al., 1984; Roldán-

62   Arjona and Pueyo, 1993). In addition, samples separated with MEI are typically washed with

63   acetone, and the mixture of these chemicals is highly flammable. Burning MEI has the potential

64   to produce large amounts of free iodine, which also poses a significant health risk (Hauff and

65   Airey, 1980). Due to its toxicity, MEI must be used in a vent hood with proper personal

66   protective equipment (PPE) and requires special training in safe handling techniques (Dumitru

67   and Stockli, 1998).

68   Safety precautions required for hazardous chemical handling may exclude workers or

69   students with conditions that do not allow them to comply with the safety precautions. For

70   example, personal protective equipment may only be available in restricted sizes, and fume hood

71   design is often incompatible with the use of wheelchairs or other mobility devices. Thus,

72   eliminating hazardous chemicals from laboratory procedures results in both a safer work

73   environment and a more inclusive workplace.

74   Many labs elect to use lithium heteropolytungstate (LST), lithium metatungstate (LMT),

75   and sodium polytungstate (SPT) because they are generally non-toxic and relatively inert

76   (Munsterman and Kerstholt, 1996; Mountenay, 2011). Similar to bromoform (but less toxic)

77   these heavy liquids can be used at densities of 2.8-3.0 g/cm^3 to remove quartz and feldspar from

78   the separate, but they do not separate apatite from zircon. Zircon and apatite crystals in natural

79   samples exhibit a wide variety of morphologies depending on the lithology, sample history, or

80   mineral separation methods used. In many cases, zircon and apatite crystals can be identified by

81   eye under a binocular microscope based on crystal habit and relief. Optical methods such as

82   crossed polarizers can be used in addition to crystal shape to distinguish these phases from each

83   other as well as from other phases such as titanite, xenotime, monazite, allanite, rutile,

84   baddeleyite, etc. However, it is not uncommon for a sample separate to include grains with sub-

85   optimal morphologies, surface pitting, and broken surfaces which make correct mineral

86   identification a challenge even with the procedures described above. The challenge is greater in

87   labs that include personnel inexperienced at picking and/or a suboptimal microscope set-up.

88   Mistaken mineral identification can lead to significant issues in data analysis, quality, and

89   interpretation. Depending on the geochronologic technique employed, this misidentification

90   might be detected further along in the analytical procedures. In (U-Th)/He analysis, a mistake

91   may be realized during degassing or dissolution. Due to their different diffusion behavior, zircon

92   usually requires higher temperatures and longer laser-heating times to fully extract He than for

93   apatite (e.g. Farley, 2002). Apatite dissolves readily in a weak nitric acid, whereas zircon needs

94   to be subjected to extensive Parr bomb pressure dissolution procedures using a mixture of nitric

95   acid, hydrochloric acid, and hydrofluoric acid to be completely dissolved (Farley, 2002). As a

96   result, a misidentified mineral may not be completely degassed or dissolved during the analytical

97   procedure, leading to erroneous results. The presence of Ca or Zr in dissolved mineral solutions

98   can be used during subsequent isotope-dilution ICP-MS analysis to test whether the correct

99   phase was chosen for the analysis, as was demonstrated for (U-Th)/He by Guenthner et al.

100   (2016).

101   Similar issues arise in other methods. In laser ablation analysis as part of U-Pb or (U-

102   Th)/He dating, the ablation characteristics and the presence of Ca or Zr in the analyte can be used

103   as diagnostic criteria. Etching parameters for fission track, such as the type and molarity of acids,

104   etching time, and temperature conditions, are highly phase-specific and need to be tightly

105 controlled to yield reproducible and internally consistent data (Tagami and O'Sullivan, 2005).

106 Applying zircon etching procedures to apatite grains might lead to the complete loss of a sample.

107   Given the amount of time and materials required by these analytical methods,

108 misidentification of minerals can lead to significant monetary and time-effort losses. Many

109 laboratories will use techniques to reduce mineral misidentification for challenging samples.

110 These can include having a more experienced user look over selected grains, analyzing pre-

111 selected grains under a scanning electron microscope (SEM) to measure elemental compositions

112 with energy dispersive spectroscopy (EDS), using Raman spectroscopy for phase identification,

113 and others. Which of these techniques is employed at a given institution varies based on

114 instrument availability, budget, and time allotted for this task.

115   Here we show that X-Ray micro-computed tomography (microCT) scanning can be used

116 as an effective pre-screening tool to distinguish between apatite and zircon and to detect

117 misidentification of grains. MicroCT is growing in popularity in Earth science departments as

118 benchtop systems make operations simpler and more affordable. Many universities already have

119 microCT instruments available in engineering or health sciences departments.

120   The difference in apatite and zircon composition and densities (3.1-3.2 g/cm^3 and 3.9-4.7

121 g/cm^3, respectively) lead to differential X-ray absorption, which yields characteristic grayscale

122 value contrast in microCT data (e.g. Ketcham and Carlson, 2001). In addition to phase

123 identification, microCT data yields high-resolution 3-dimensional grain shape measurements and

124 reveals internal heterogeneities, such as fractures or inclusions (Evans et al., 2008; Glotzbach et

125 al., 2019; Cooperdock et al., 2019). Resolution varies by instrument and acquisition parameters;

126 the instrument used in this study achieves a maximum voxel resolution of ~2 $\mu m/10$ μm^3. We

127 explore different acquisition parameters to optimize the distinction between different minerals

128 and minimize the scan time to yield a streamlined procedure for routine pre-screening of mineral

129 grains for geochronologic applications.

130 **2 Materials and methods**

131 **2.1 Mineral separation**

132   We selected Fish Canyon Tuff (FCT) as a test sample because it contains both apatite and

133 zircon and is used as an age standard in many applications of geo- and thermochronology

134 (McDowell et al., 2005; Donelick et al., 2005). We obtained three separate FCT samples: one

135 mineral separate of a MEI heavy fraction given to us by the UTChron Laboratory at the

136 University of Texas at Austin (UT-FCT), and two that we collected from two FCT localities near

137 Monte Vista, CO (USC-FCT1: 37° 36' 38.73" N, 106° 42' 19.93" W; USC-FCT2: 37° 38'

138 22.21" N, 106° 17' 57.77" W). The two whole-rock samples were crushed on a jaw crusher and

139 disk mill at the University of Southern California. Crushed samples were sieved and the 75-250

140 μm size fraction was washed before using a hand magnet and a Frantz isodynamic magnetic

141 separator to remove magnetic fractions. Samples then underwent density separation using lithium

142 heteropolytungstate (LST). This is a water-based, low-toxicity heavy liquid with a maximum

143 density of 2.85 g/cm^3 at room temperature that produces a heavy mineral separate with apatite

144 and zircon (and other phases) mixed together. Sample types and names are summarized in Table

145 1.

146   The UT-FCT separate supplied by the University of Texas at Austin was processed using

147 the same mineral separations procedures with the following exceptions: the samples were density

148 separated on a Gemeni water table prior to magnetic separation, and the sample experienced a

149 two-step heavy liquids separation using bromoform and MEI. These heavy liquids are more toxic

150 than LST but have densities of 2.95 g/cm^3 and 3.32 g/cm^3, respectively, and should yield grain

151 fractions that separate apatite from zircon. Only the MEI heavy fraction was used for this

152 experiment.

153   As a reference for microCT imaging, we used mineral standards for apatite, zircon, and

154 titanite from existing collections. Two Durango apatite standards from large apatite crystals were

155 supplied by the UTChron laboratory at the University of Texas at Austin (UT-DUR) and Caltech

156 (ClT-DUR). We used shards from large crystals of Sri Lankan zircon (SL1) from Caltech (Farley

157 et al., 2020) and Minas Gerais titanite (MG1) from the Natural History Museum of Los Angeles

158 County (more specific sample location information is not known). These standard crystals were

159 gently hand crushed and sieved to <75 μm, 75-250 μm, and >250 μm size fractions.

160

161 Table 1. Mineral standards and unknowns used in this study. Large standard crystals were

162 crushed to obtain shards to be used as a reference for microCT analyses. Unknown grains were

163 extracted from FCT whole-rock samples.

Sample	Minerals	Type	Grain type	Sample Name	Density Separation
UT-DUR	Apatite	Standard	Shard	Durango	none
ClT-DUR	Apatite	Standard	Shard	Durango	none
SL1	Zircon	Standard	Shard	Sri Lanka	none
MG1	Titanite	Standard	Shard	Minas Gerais	none
UT-FCT	Apatite, Zircon	Unknown	Grain	Fish Canyon Tuff	bromoform, MEI
USC-FCT1	Apatite, Zircon, Titanite	Unknown	Grain	Fish Canyon Tuff	LST
USC-FCT2	Apatite, Zircon, Titanite	Unknown	Grain	Fish Canyon Tuff	LST

164

2.2 Making crystal mounts

166   Graduate students were tasked with picking mineral grains that looked like apatite or
167 zircon and covered a range of grain sizes and morphologies from the three FCT samples using a
168 Nikon SMZ25 optical microscope. It is notable that all samples, including the MEI separate,
169 yielded both apatite and zircon. The selected grains were placed onto grain mounts for microCT
170 analysis (see Sect. 2.3). Each mount also included known mineral standards for reference and
171 normalization (Fig. 1a). Three grain mounts were constructed (Mount A, B, and C, see Fig. 2).
172 Mount A included 36 grains from UT-FCT "unknowns," 10 shards of SL1 zircon, and 15 shards
173 of ClT-DUR apatite. Mount B included 39 grains of USC-FCT1 "unknowns," 32 grains of USC-
174 FCT2 "unknowns," 9 shards of SL1 zircon, and 24 shards of UT-DUR apatite. Mount C included
175 11 shards of SL1 zircon, 15 shards of CIT-DUR apatite, and 15 shards of MG1 titanite standards.
176 We used the 75-250 µm size fraction and >250 µm size fractions of the mineral standards to test
177 the impact of grain size on grayscale values in microCT data. On Mount C, individual shards
178 from each mineral were distributed evenly across the mount to test whether there is any spatial
179 variability in X-ray attenuation and grayscale.
180   We assembled grain mounts by cutting small plastic shapes (rectangles, squares, or
181 circles) out of 1 mm thick plastic slides and placing double-sided adhesive tape on one side.

7

182 Mounts for vertical scans (when the mount is standing upright on the top of the sample holder)

183 were constructed by cutting ~3 mm by 4 mm rectangles from plastic slides of 1 mm thickness,

184 which was covered with double-sided adhesive tape. Grains were placed on the upper part of the

185 rectangle mount (Fig. 1a), and the end without grains was inserted into dental wax to hold the

186 mount in place, vertically, on top of the sample holder (Fig. 1b). We tested different brands of

187 double-sided adhesive tape and found that some brands appear clear under a transmitted light

188 microscope while others have significant interference colors and visible fibers. Double-sided

189 tape selection did not affect microCT data.

190   Prior to placing the grains, the plastic mounts were temporarily secured to a glass slide

191 with double-sided tape to hold them in place. Individual crystals were selected from mineral

192 separates and placed on the tape using tweezers and needles under a light microscope. Grains

193 were spaced to avoid touching, with up to 104 total crystals per mount. Optical micrographs of

194 the mount and each individual crystal were taken with transmitted and reflected light as well as
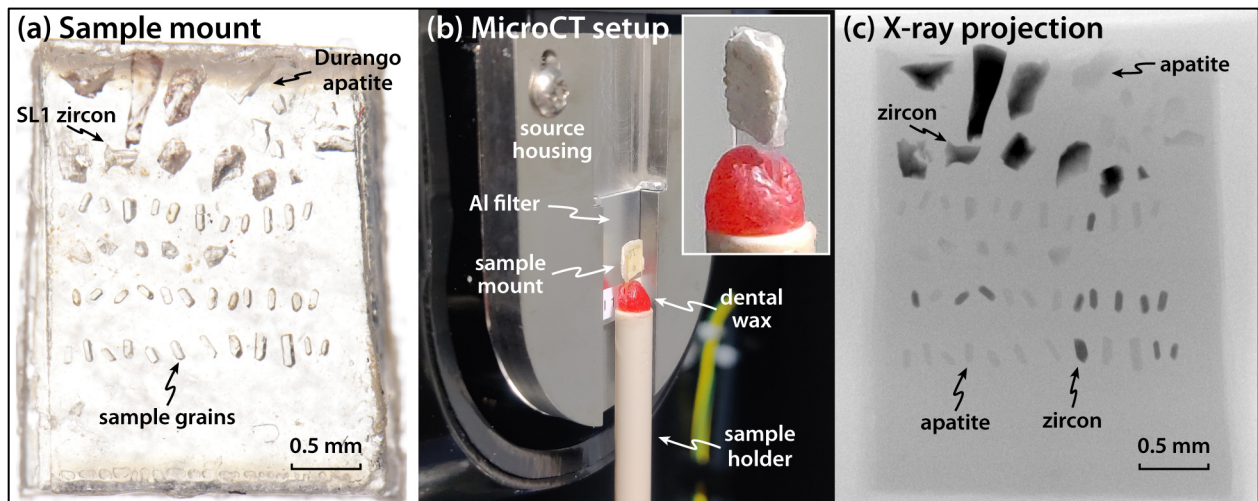
195 with crossed polarizers.

196

198 Figure 1: (a) Transmitted light micrograph of a sample mount with known apatite and zircon

199 standard shards and unknown sample grains made from a plastic slide and double-sided tape,

200 about 3 mm in width. (b) Sample mount installed vertically in the microCT instrument secured

201 on top of a sample holder with dental wax. Insert shows a closer view of the sample mount in

202 measurement position. (c) X-ray projection of the same mount as in (a). Zircon grains show up as

203 darker (more X-ray absorption) than apatite grains. The brightness in projections is controlled by

204 the material-specific X-ray attenuation as well as by the integrated thickness of the traversed

205 material.

2.3 MicroCT scanning

207   All microCT scans were acquired on a Rigaku CT Lab HX130 benchtop microCT

208 instrument at the USCHelium Laboratory at the University of Southern California. Individual

209 mounts were installed vertically (perpendicular to the X-ray beam direction, parallel to the

210 detector plane; see Fig. 1b) in order to minimize the effect of interference from X-ray artifacts

211 such as shadowing between individual grains due to beam hardening and photon starvation (see

212 Section 3.2 and Fig. 7). Mounts were scanned at accelerating voltages of 130 and 60 kV with

213 currents of 61 and 133 μA, respectively. We used a 1.0 mm thick aluminum filter to selectively

214 remove lower energies from the polychromatic beam in order to reduce the effect of beam

215 hardening (see Hanna and Ketcham, 2017, for details). Total instrument run times were between

216 18 seconds and 125 minutes using continuous and step scanning with a field of view (FOV) of 5

217 mm diameter and 3.8 mm height (see Table 2). Continuous scans were done for 18 seconds, 4

218 minutes, 17 minutes, and 68 minutes. Over this time, the sample is rotated and X-rays are

219 continuously counted on the detector. We also performed 125-minute step scans (500 ms

220 exposure time, 1500 projections, 4 integrations), in which the sample is rotated in steps and the

221 detector moves between the steps to reduce ring artifacts. As a result, the 125-minute scan time

222 includes 50 minutes of actual X-ray exposure and 75 minutes of instrument adjustment. Note, in

223 continuous scans the scan time and exposure time are the same because there is no detector

224 adjustment. We report the total instrument scan time in Table 2 and the total exposure time on

225 Figure 7. Reconstructions were computed using the Rigaku CT Reconstruction software.

226 Continuous scans were reconstructed to yield volumes with a width and length of 1024 voxels.

227 Step scans were integrated for longer times than the continuous scans and yielded enough data to

228 be processed at full resolution (width/length of 2784 voxels) while maintaining a usable signal-

229 to-noise ratio.

230

231 Table 2. Scan parameters tested in this study.

Scan voltage (kV)	Scan type	Total scan times	Voxel size (μm)	Volume size (pixels)	File size (GB)

		(minutes)			
60 and 130	continuous	0.3, 4, 17, 68	5.7	1024x1024x708	1.4 (0.2 cropped)
60 and 130	step	125	2.1	2784x2784x1931	27.8 (2.4 cropped)

2.4 MicroCT data analysis

The reconstructed microCT data was processed with Dragonfly (Version 2021.1) by Object Research Systems. Reconstructed volumes of each mount with all different scan times and X-ray energies were loaded into Dragonfly. The volumes scanned at 60 kV for 68 min were used as a reference since they displayed the best signal-to-noise ratio of all the tested scan parameters. Volumes were registered relative to the 60 kV/68 min scans using the Image Registration tool, which translates and rotates volumes to align scans. Grains were segmented in the 60 kV/68 min scan volumes by creating regions of interest (ROI) using histographic segmentation, which delineates grains from their surroundings (air or adhesive tape) based on threshold grayscale values. The resulting volumes were filtered by applying a 3D opening operation (a combination of erosion and dilation which removes small objects, like dust, while not changing the geometry of large volumes) and eroded by one voxel to remove the effect of rapid changes in grayscale value near the grain boundary.

Each grain was separated into an 'object' by creating a Multi-ROI (a ROI that contains multiple objects) from continuous segments in which voxels are connected by at least one of their faces (6-connected). Each grain 'object' consists of hundreds to thousands of voxels that can be used to calculate grayscale statistics. Small fragments separated from larger grains of less than 100 voxels were not used for further analysis to ensure the measurements have statistical significance. In this way, individual grains were mapped out and distinguished from other small objects in the scan (e.g., chipped pieces or detritus on the adhesive tape). The geometry of the segmented objects was resampled to fit each volume, and information on the position, size, surface area, and greyscale value distribution of each grain was extracted from the Multi-ROIs.

Absolute grayscale values can change between scans since they are dependent on the scan geometry, acquisition parameters, arrangement of grains, and processing, with internal normalization and scaling being applied during reconstruction. To make scans comparable, we chose to normalize the grayscale values of all grains on a mount by the average grayscale value of the SL1 zircon grains in the same volume. We also computed the ratio of the grayscale values

259 of the 60 kV and 130 kV scans with otherwise identical scan parameters to yield a dual-energy

260 parameter.

261 **2.5 Phase validation by Raman spectroscopy**

262   To validate the different phases observed in microCT data, we determined the mineral

263 phase of 35 grains in Mounts A and B by Raman spectroscopy. This included a subset of 28

264 unknown grains from FCT samples and 7 shards of known mineral standards (Fig. 2).

265 Representative grains were selected to encompass a range of grain sizes and morphologies,

266 positions on the mount, and microCT grayscale contrast. After microCT scanning, the grain

267 mounts were transferred to a glass slide, and grains were analyzed using a HORIBA XploRA

268 PLUS spectrometer at the Natural History Museum of Los Angeles County. Apatite, zircon, and

269 titanite were identified by matching baseline-corrected spectra with comparison spectra from the

270 RRUFF database (Lafuente et al., 2005) using CrystalSleuth. Raman spectral analyses were

271 conducted using a green 532 nm diode laser at 50% laser power, a diffraction grating of 1880

272 gr/mm, a 100x (0.9 NA) objective, 200 μm slit, and 300 μm pinhole for confocal optical

273 geometry. Raman spectra were collected in the range of 100-1600 cm^{-1} with each grain analyzed

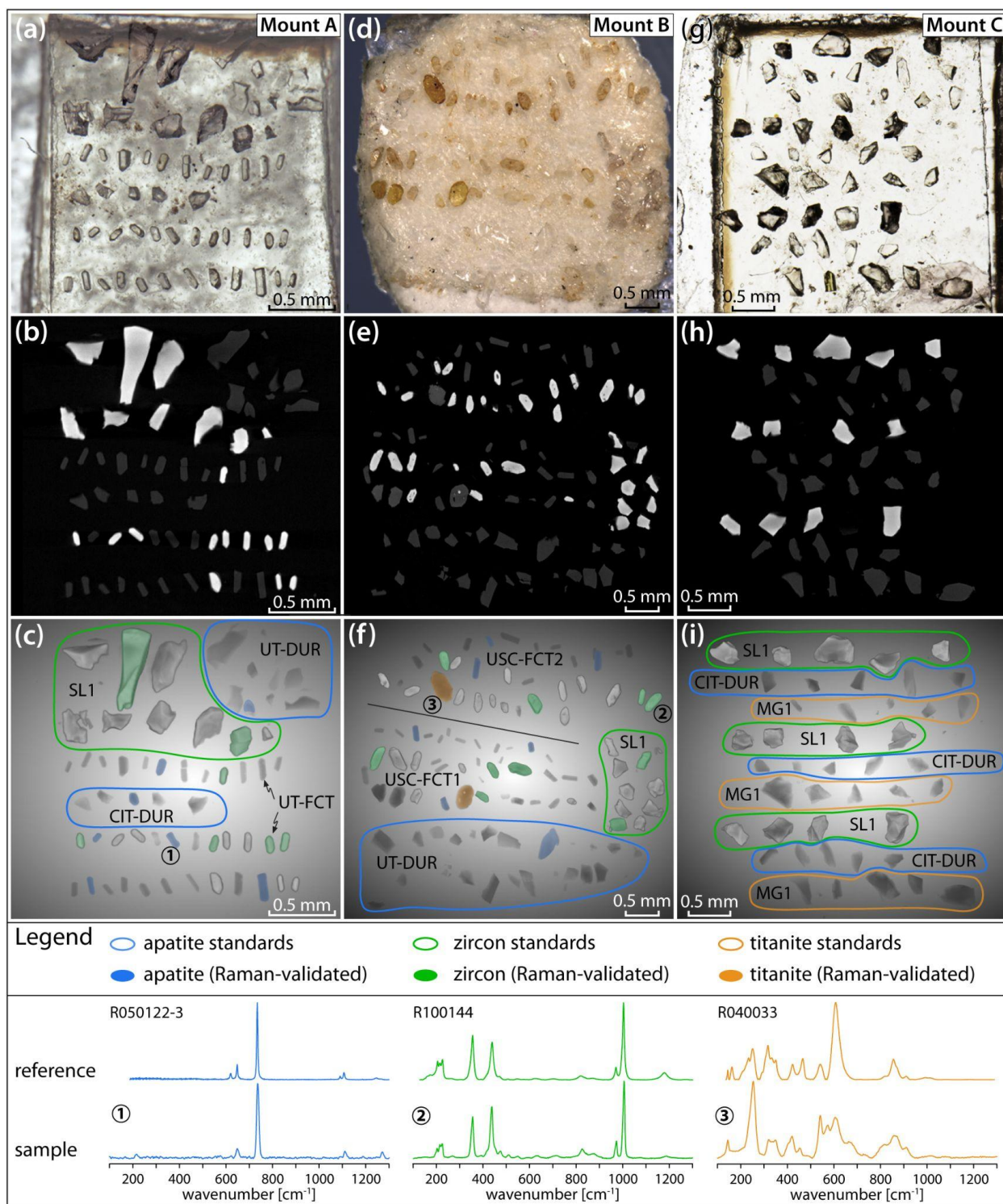274 with a 3 s exposure averaged from 10 acquisitions.

275

276

277

Figure 2: Transmitted light micrographs (a,d,g), microCT slices (b,e,h), and microCT volume renderings (c,f,i) of Mounts A, B, and C. MicroCT slices show a large contrast between apatite/titanite (darker) and zircon grains (brighter). Grayscale color and grain relief in 3D renderings are distinct for different mineral phases. The 3D renderings show Raman-validated

283 grains highlighted and known standard shards circled in blue (apatite), green (zircon), and

284 titanite (orange). Baseline-corrected Raman spectra of representative grains and reference spectra

285 from the RRUFF database (including record numbers) are shown below the images. Numbers in

286 circles indicate the grains in the volume renderings which correspond to the sample Raman

287 spectra.

288 **3 Results and discussion**

289   Different microCT scanning parameters were systematically tested on the same three

290 grain mounts to determine the optimal scan conditions for distinguishing between mineral phases

291 while minimizing cost, time, and data file sizes. Individual microCT data file sizes range from 2

292 to 28 GB depending on acquisition and processing parameters. Reconstructing and manipulating

293 large datasets can require specialized computers with demanding system requirements for data

294 storage, memory, and processing power. The microCT data for single grain mounts, like the ones

295 used in this study, can be cropped to produce manageable file sizes that can be viewed and

296 analyzed without the need for specialized computers. We determined that for the instrument used

297 here a continuous scan time of 17 min at 60 kV (5.7 μm resolution) is sufficient for mineral

298 identification between apatite and zircon. For phase identification plus high-resolution surface

299 area and volume for 3D grain geometry measurements (as is typical for (U-Th)/He

300 thermochronology), we recommend using a 125 min step scan at 60 kV (2.1 μm resolution).

301 These parameters are optimized for apatite and zircon and can be modified for other minerals of

302 interest. Below, we evaluate the effects of X-ray energy, grain size, and spatial distribution on

303 quantitatively distinguishing zircon from apatite using microCT data.

304 **3.1 Theoretical X-ray attenuation**

305   We calculated the theoretical X-ray total attenuation coefficients of apatite, zircon,

306 titanite, monazite, and rutile (Fig. 3a) for a range of X-ray energies commonly used for microCT

307 (~30-230 keV) using MuCalc (https://www.ctlab.geo.utexas.edu/software/mucalctool/), a

308 Microsoft Excel plugin which uses data from the NIST XCOM database of mineral-specific

309 parameters (Hanna and Ketcham, 2017). The modeled attenuation coefficients predict how X-

310 rays interact with different minerals. The greater the difference in attenuation coefficients, the

311 more distinct two mineral phases will appear in microCT data.

312   Based on these calculations, zircon has a much higher attenuation coefficient than apatite

313   across the energy spectrum. At lower energies, the difference between the attenuation

314   coefficients of other minerals relative to zircon (Fig. 3b) is greater than at higher energies. The

315   attenuation coefficients of apatite, zircon, titanite, and rutile converge around 200-300 keV.

316   Thus, energies less than ~200 keV should make zircon grayscale values distinguishable from

317   apatite and other lower attenuation phases (i.e., zircon appears brighter in reconstructed microCT

318   data as seen in Fig. 2). The attenuation coefficients of apatite and titanite are similar at all

319   energies, but display slightly more divergence <80 keV. The observed X-ray attenuation of

320   actual mineral grains might differ from these predictions due to material inhomogeneity,

321   compositional variation (such as endmember mixing and elemental substitution), crystal defects

322   (e.g., metamictization), inclusions, and artifacts due to shadowing from neighboring grains

323   (photon starvation) and beam hardening. In this study, we analyzed our mounts at the maximum

324   achievable voltage on the Rigaku CT Lab HX130 of 130 kV as well as a reduced voltage of 60

325   kV. These parameters may vary for other microCT instruments.
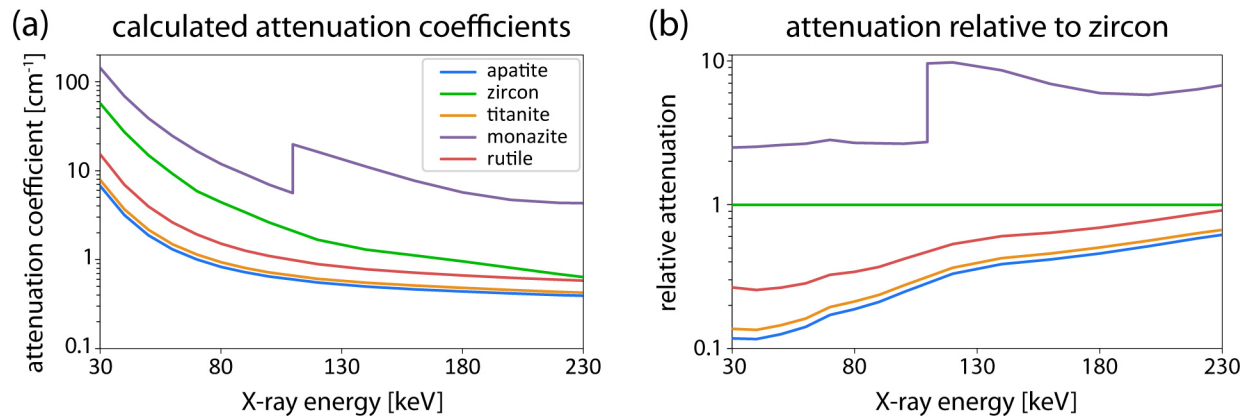
326

327

328

329   Figure 3: (a) Attenuation coefficients for commonly dated minerals over a range of X-ray

330   energies calculated with MuCalc. (b) The same modeled attenuation coefficient data normalized

331   by zircon. Generally, higher attenuation coefficients mean brighter grayscale values in

332   reconstructed microCT data. A greater difference in attenuation coefficients between mineral

333   phases aids in mineral identification.

334

3.2 Normalized grayscale values of grains

We use the 68-minute continuous scans to assess how grayscale values of individual grains (or shards) vary at different scan energies and for different mineral phases. Grayscale values for individual grains of unknowns and standards were normalized by the average value of the SL1 zircon shards on each mount for each set of scan parameters. The absolute grayscale value in the volumes depends on scanning conditions and reconstruction settings, thus internal normalization makes the results comparable and independent of these parameters.

We found that apatite grains have grayscale values of about 22% and 27% (at 60 kV and 130 kV, respectively) of those of zircon grains (Fig. 4). The distributions are broad due to intra-grain, inter-grain, and inter-sample variability, but the apatite and zircon populations are distinct from each other so that individual grains can be uniquely identified. This also confirms the theoretical modeling (Fig. 3) and the observations of different X-ray attenuation of apatite and zircon grains in the X-ray projections (Fig. 1). The grayscale value distribution of titanite overlaps partially with that of apatite and is sample-dependent, making a phase distinction possible for some but not all grains. For example, the MG1 titanite mineral standard more closely overlaps the apatite grains than the "unknown" titanite crystals picked from USC-FCT1 and 2, which are systematically slightly brighter (Fig. 5).

The separation between all of the distributions is greater for 60 kV than for 130 kV, as predicted by the theoretical modeling above (Fig. 4). Therefore, volumes from scans at 60 kV can be used to resolve smaller differences in X-ray attenuation than at 130 kV, which does not have a pronounced effect on the apatite-zircon distinction but can be useful when trying to distinguish between apatite and titanite. However, lower energy X-rays are less penetrating and lead to more artifacts and noise in the resulting reconstructed data (Hanna and Ketcham, 2017). Therefore, there is a trade-off between the absolute separation of phases in grayscale-value space and the signal-to-noise ratio, the latter of which can be improved by longer scan times.
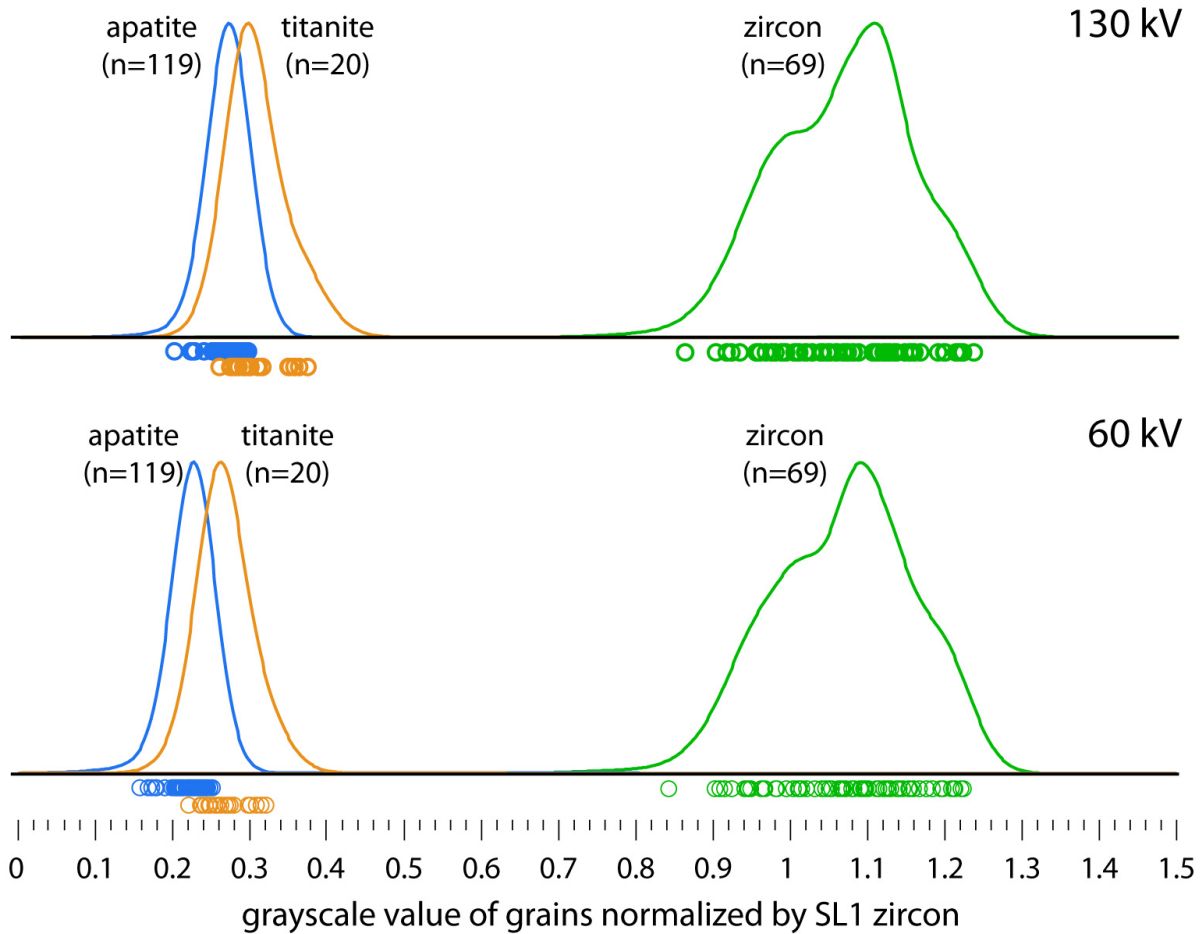
15

Figure 4: Kernel density estimates (KDEs) of all apatite, zircon, and titanite grayscale value measurements (including standards) for 68 min scans calculated with an adaptive bandwidth equal to the standard deviation of grayscale variation within each grain. Each KDE is an aggregation of data from three different sample mounts and shows all individual data points. The grayscale value of each grain was normalized by the average grayscale value of SL1 zircon grains in the same volume. The difference between the attenuation of the three minerals is greater at 60 kV than at 130 kV, as theoretically predicted.

We observed good reproducibility for average normalized grayscale values of populations of the same sample across the three mounts (Fig. 5). For example, the average normalized grayscale values of Durango apatite shards (UT-DUR) are all within uncertainty at 0.255±0.046 (2σ) for Mount A, 0.267±0.016 for Mount B, and 0.272±0.014 for Mount C. Some of these average values are skewed by individual outliers, which are likely due to grain size effects (see Section 3.4).

376   Although average grayscale values across grain populations are reproducible, we observe

377   a range of grayscale values for individual replicate grains from the same sample or of shards

378   from the same crystal (Fig. 5). This may be due to differences in bulk composition and structure.

379   For example, natural apatites are solid solutions of three different endmembers which have

380   different densities. The exact composition of any apatite grain will have an impact on its X-ray

381   absorption and hence the observed grayscale value. Zircon density is mainly controlled by

382   radiation damage (Holland and Gottfried, 1955), which can cause different densities for different

383   grains or of parts of the crystal in the case of pronounced zoning of radioactive elements. The

384   effect of differing grayscale values between different samples is most pronounced between the

385   titanite standard in Mount C and the titanite from FCT samples in Mount B (see Fig. 5). The

386   density of titanite has also been shown to be a function of crystal damage (Vance and Metson,

387   1985).

388   We segmented grains based on their outer surface and calculated the average grayscale

389   value of the material enclosed by that surface. It is necessary to exclude the outermost grain

390   boundary because it commonly appears falsely brighter due to beam hardening. However, if

391   there is internal heterogeneity, such as inclusions with higher or lower grayscale values, the

392   observed average grayscale value of any particular grain can be affected (expressed as RSDs).

393   Grains with a large fraction of inclusions of a particular type can therefore change the average

394   grayscale value and might lead to misidentification. One strategy to mitigate this would be to

395   filter certain histographic ranges of values within the segmented grains to exclude inclusions and

396   measure only the average grayscale value of the host grain. Alternatively, this could also be used

397   as a tool to identify individual crystals with inclusions, which would display higher or lower

398   average grayscale values than the rest of the population.

399   The grayscale value distribution within a particular mineral grain is dependent on the

400   natural variation of density and composition (such as zoning) as well as measurement noise. The

401   absolute 2σ-variability of apatite and titanite grains is about 0.01-0.02 for apatite and 0.1-0.2 for

402   60 kV/68 min scans normalized by SL1 zircon (Fig. 5). In relative terms, this is a 5-10%

403   variation for apatite and titanite, and a 10-20% variation for zircon. Measurement noise in the

404   reconstructions is likely not the main contributing factor to this variation in the 68 min scans (see

405   Section 3.4 and Fig. 7). The remaining variations can be due to changes in material parameters

406   across a grain, inclusions of different densities than the host phase, and beam hardening. Overall,

17

407 the normalized grayscale value can be used to distinguish apatite and zircon, and to some extent

408 other phases such as titanite. Employing strategies to minimize noise and artifacts is important to

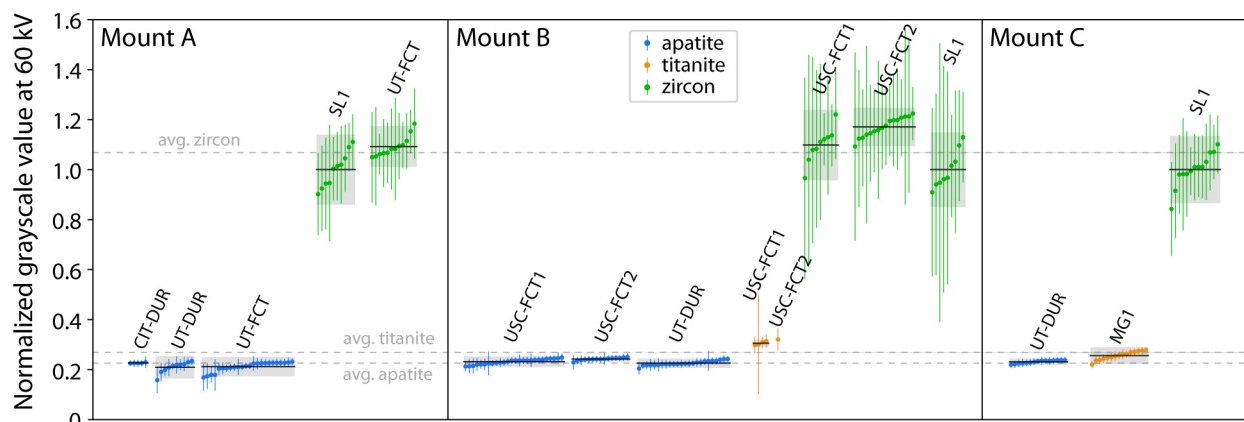409 make this distinction robust for every analyzed mineral grain.

410

411

412

414 Figure 5: Mean grayscale values (normalized by SL1 zircon) for all grains measured in 60 kV/68

415 min scans, given with 2σ-variability and organized by mount and sample. Zircon is shown in

416 green, apatite in blue, and titanite in orange, as in the other figures. The average for each sample

417 is given as a black bar with the 2σ-variability shaded in gray. Averages for the whole populations

418 of apatites, zircons, and titanites are given as gray dashed lines. Zircon and apatite populations

419 for all mounts are distinct, while apatite and titanite populations show some overlap. There is

420 observable inter-sample variability in the mean normalized grayscale value of each mineral but

421 values for the same samples (e.g., UT-DUR) are reproducible within error between mounts.

3.3 Use of dual-energy data

423   The change of the attenuation coefficient with X-ray energy is a function of material

424 density and composition, and is characteristic for each mineral (Alves et al., 2014). Therefore,

425 the ratio of the attenuation at two different X-ray energies can be used as an additional parameter

426 to identify the mineral phase of a grain (e.g. Hanna and Ketcham, 2017). We observed a clear

427 distinction between apatite and zircon in this parameter as well (Fig. 6a). Titanite again appears

428 similar to apatite, but the separation between the two distributions is greater in dual-energy space

429 than in the 60 kV or 130 kV data alone. Therefore, this dual-energy parameter can be used as an

430 additional tool to distinguish phases that have similar absolute attenuation coefficients, and

431 hence appear similar in terms of grayscale values. This necessitates two scans of the same mount

432 at two different energies, as well as additional processing to align the two scans and compute

433 average grayscale values for both scans. However, the resulting data can be used to map regions

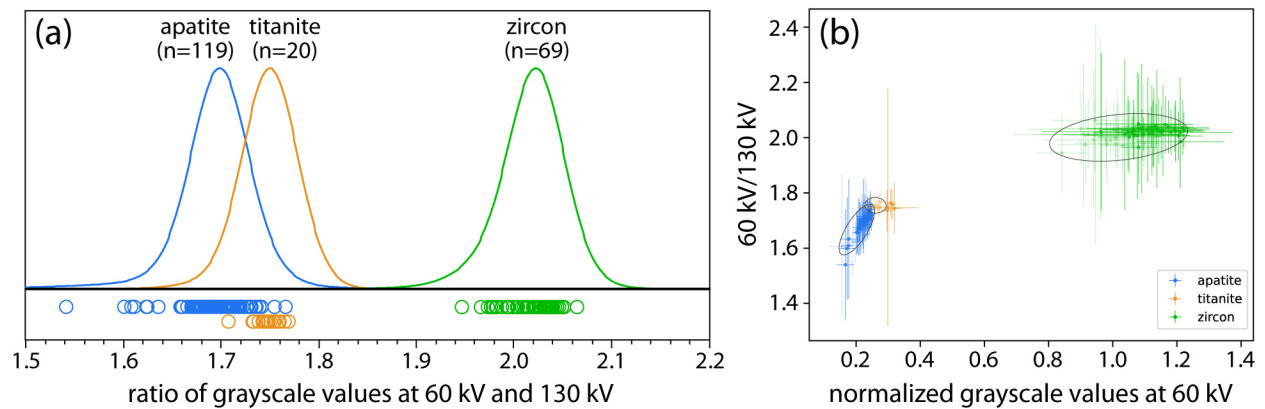434 in dual-energy vs. single-energy plots (Fig. 6b), yielding a more robust phase identification for

435 individual grains.

436

437

438

439 Figure 6: (a) Kernel density estimates of the ratios of the grayscale values at 60 kV and 130 kV

440 for grains from all three mounts. The mounts were scanned at 60 kV and 130 kV with otherwise

441 identical scan parameters and the grayscale values were measured at the same positions. Zircon

442 and apatite form very distinct distributions, and the populations of apatite and titanite overlap but

443 show more separation than grayscale values from scans at a single energy. (b) Dual-energy

444 parameters plotted against normalized grayscale values at 60 kV. Known standards are shown in

445 lighter colors and black lines outline the field of values of standards. Unknown sample grains of

446 apatites and zircons fall almost entirely within the field of standards. Titanite sample grains are a

447 significantly different brightness (grayscale values) than sample grains but have the same dual-

448 energy parameter.

449

450 **3.4 Optimizing mount geometry and scan parameters**

451   We tested the grayscale variability introduced by grain size, spatial distribution of the

452 grains on a mount, and direction of the mount during microCT data acquisition. Each of these

453   factors can affect the path that X-rays take through the grains and the preferential attenuation of

454   parts of the X-ray spectrum of a polychromatic beam (beam hardening), which can result in

455   artifacts that cause changes of the average grayscale for a given grain unrelated to the actual

456   mineral-specific X-ray attenuation. We found that image quality and signal-to-noise ratio

457   improved with increased scan time (Fig. 7), as is expected based on counting statistics. We

458   quantified variability in our data by calculating the relative standard deviation (RSD) of

459   grayscale value within each segmented grain, which is a measure of both natural variability of

460   the material and any superimposed measurement noise.

461   A clear distinction between apatite and zircon can already be observed in the 18 s scans

462   (Fig. 7), although the RSDs are high (0.2-0.3) for both apatite and zircon grains. The RSDs

463   decline with increasing scan time for otherwise constant experimental conditions (Fig. 6),

464   asymptotically approaching ~0.04 for apatite and ~0.08 for zircon. The remaining RSDs might

465   reflect the true natural variability of material parameters (density, endmember mixing, crystal

466   damage, elemental substitution, inclusions) within the mineral grains. For the particular

467   instrument and experimental setup employed here, the signal-to-noise ratio did not improve

468   significantly beyond a scan time of 17 min at a reduced resolution (voxel size of 5.7 μm). For

469   full-resolution reconstructions, a 125 min scan time was sufficient to produce comparable RSDs,

470   while also allowing for a smaller voxel size (2.1 μm) which is preferable for obtaining geometric

471   parameters, such as crystal size and shape for FT-corrections (Evans et al., 2008).

472   We also found that the orientation of the mount during data acquisition has a significant

473   effect on the data quality. A vertical orientation, perpendicular to the source and parallel to the

474   detector plane, produced much lower RSDs for the same scan conditions than a horizontal

475   position (Fig. 8). Highly attenuating phases (such as zircon) produce artifacts such as shadowing

476   and streaking (e.g. Hanna and Ketcham, 2017). When these artifacts overlap with other sample

477   grains, they can significantly alter the observed grayscale value of parts of grains which does not

478   reflect their actual X-ray attenuation and leads to erroneous measurements with increased RSDs

479   (Fig. 8). X-rays passing through a horizontal mount traverse several grains in most orientations

480   and produce strongly expressed artifacts, whereas data acquisition in a vertical position

481   significantly decreases the number of rays that pass through more than one grain. Therefore,

482   particularly for samples with highly attenuating phases, we recommend scanning mounts in a

483   vertical position to reduce noise and improve reproducibility. A tilted orientation can achieve

484   similar results but makes data cropping more difficult. Scanning mounts horizontally is another,

485   more common option that may be suitable depending on the phase of interest.

486   The size and arrangement of the grains on the mount also had an influence on the

487   observed grayscale values and their RSDs. We tested these effects with a grain mount (Mount C)

488   composed of only shards of known standards (apatite, zircon, and titanite). For a vertical scan,

489   the horizontal position did not have an observable effect on the measured grayscale values of

490   grains (Fig. 8a) but the vertical position did have a significant effect, with grayscale values

491   decreasing downwards (Fig. 9b). This effect was observed for both apatite and zircon. Titanite

492   showed an even greater dependence on the vertical position, but this trend was exaggerated by

493   the predominance of smaller shards in the top row and larger ones in the bottom row of the

494   mount. These spatial effects are likely caused by the inhomogeneity of the total X-ray

495   attenuation at any height above the sample holder due to clustering of grains at certain heights.

496   These spatial effects can be minimized by distributing known standards throughout the grain

497   mount and normalizing sample grain measurements by the closest standard, and by avoiding

498   lines or grid shapes when placing grains.

499   We observed a general trend of decreasing grayscale values with increasing grain size for

500   the set of all grains of this mount (Fig. 9c). This trend can be explained by beam hardening (see

501   Hanna and Ketcham, 2017), which results from the preferential attenuation of low-energy parts

502   of the X-ray spectrum by highly attenuating material. This effect makes the center of highly

503   attenuating regions appear darker. This artifact can lower the observed average grayscale value

504   of a grain, producing measurements that are not solely related to the attenuation coefficient of a

505   phase. This can be counteracted by choosing standard grains/shards that are matched in size to

506   the unknown sample grains. If beam hardening occurs, it will affect all grains equally, thereby

507   allowing for a direct, unbiased comparison of the average grayscale values of sample grains and

508   standards.

509   The geometric effect discussed above can change the average observed grayscale values

510   of grains by 5-10%. Even with these effects, apatite can still be distinguished from zircon due to

511   their large relative difference in X-ray attenuation. However, precautions should be taken when

512   distinguishing apatite from titanite, which displays a much lower relative contrast (see Figs. 4, 5,

513   6), to ensure that data quality is high and phase identification is robust and unique.
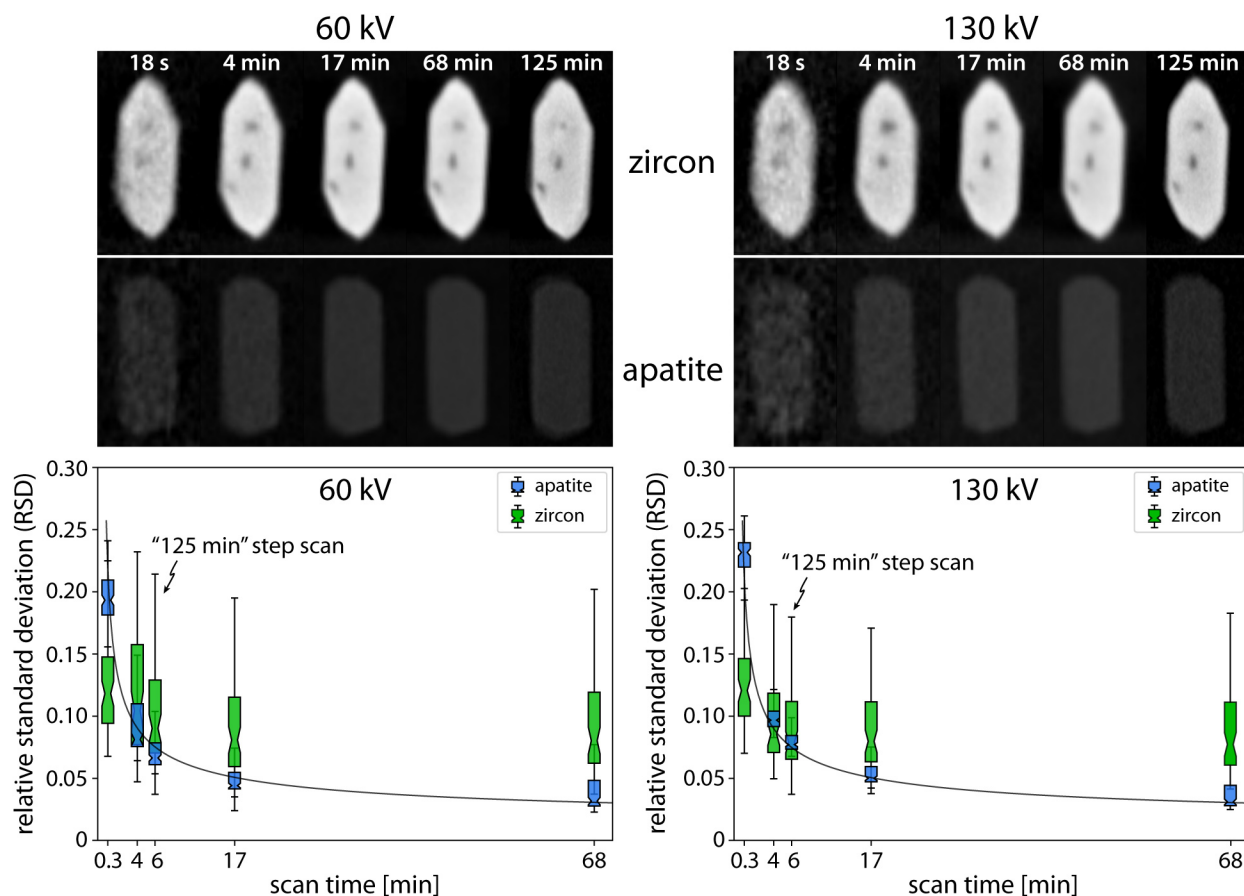
514

Figure 7: Slices of selected grains (top) and grayscale relative standard deviations (RSDs) of all analyzed apatite and zircon grains (bottom) at different scan times for 60 kV and 130 kV scans. Slices are given at the same contrast settings, showing the difference in grayscale value between apatite and zircon. Scans of 18 s, 4 min, 17 min, and 68 min are processed at a reduced resolution (5.7 µm) whereas 125 min scans are processed at full resolution (2.1 µm). Image quality and signal-to-noise ratio improve with longer scan times, and graphs of $1/\sqrt{n}$-functions are given for reference (gray lines). For our instrumental and scan parameters, we did not see significant improvements in signal-to-noise ratio past 17 min.
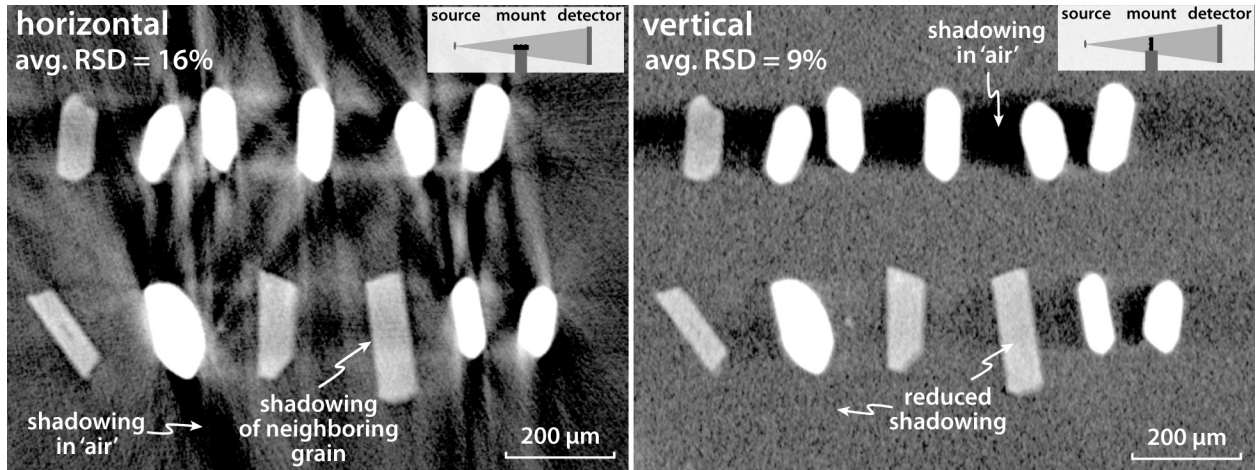
Figure 8: Slices of horizontal and vertical scans of the same grain mount show the reduction of artifacts for the vertical scan position relative to the horizontal scan position. Highly attenuating zircon (bright) grains produce shadowing artifacts that overlap with apatite (less bright) grains, altering the overall grayscale value measured in the apatite grains. Some shadowing still occurs in the vertical position but is much reduced relative to the horizontal position. This is reflected in the relative standard deviation (RSD) of the grayscale value within each set of grains. The arrangement of grains in a geometric pattern leads to the amplification of artifacts. Note: Photographs have increased contrast to highlight the differences in artifacts.
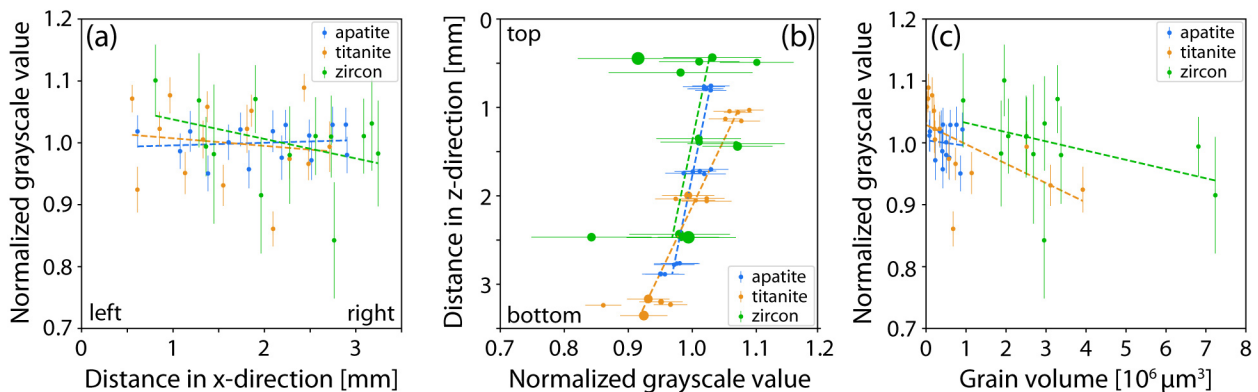

Figure 9: Plots showing the effect of spatial parameters on the grayscale values of the grains on Mount C, which contains shards of known apatite, titanite, and zircon crystals (see Fig. 2). The measured grayscale values have been normalized by the average of all grains of that mineral. Linear regressions (dashed lines) show approximate trends. (a) There is no systematic variation of normalized grayscale values with horizontal distance (x-direction) of grain placement on the

542 mount. (b) The normalized grayscale values of all mineral grains show a dependence on vertical
543 distance (z-direction) on the mount. The trends of decreasing brightness from top to bottom are
544 roughly parallel for apatite and zircon, with around 5% total variation. Titanite shows larger
545 grayscale variations (~10%), which are partly due to variations in the volume of grains (size of
546 symbol correlates with volume). Larger grains are preferentially located at the bottom of the
547 mount, thereby amplifying this trend. (c) Grains of larger volume have lower grayscale values,
548 likely due to the effects of beam hardening.

549 **3.5 Recommended procedures for microCT phase identification for geo- and**
550 **thermochronology**

551 Based on the calibrations above, we share a workflow that allows the identification of apatite and
552 zircon grains in grain mounts for geo- and thermochronology using microCT. The same dataset
553 can be used for grain-specific 3D inclusion mapping, surface area, and volume measurements.
554 The methodology described here has the potential to eliminate the need for highly toxic heavy
555 liquids (MEI and bromoform), reduce time spent picking grains, and curtail misidentification of
556 apatite and zircon in geo- and thermochronological analyses. Instead, this enables users to
557 quickly pick suitable-looking grains without close visual inspection and appraisal of interference
558 colors, crystal shape, etc., in mixed apatite and zircon separates after using less toxic heavy
559 liquids (LST, LMT, SPT). This can reduce the time spent on the microscope, particularly for
560 'difficult to pick' samples, such as those with very challenging grain morphologies or large
561 volume separates. Although not done in this study, it is conceivable to sprinkle a mineral
562 separate onto adhesive tape and use microCT to scout (bright) zircon grains prior to more
563 directed picking or LA-ICP-MS. This approach may also be preferable in cases in which
564 microscope picking is not an accessible task (e.g., due to the physical set up, frequent migraines,
565 etc.).
566 We found that using clear plastic slides (thickness ~0.5 mm) as a base for grain mounts
567 provided the necessary rigid support to hold the grain mounts in place while handling during
568 microCT scanning. These plastic slides have a similar refractive index to glass and can be easily
569 cut with scissors or other implements. Exact mount shapes (circles, squares, rectangles) depend
570 on the scanner set-up. Generally, the goal is to maximize the grain mount surface area to fit a
571 large number of grains on a single mount. As mentioned, double-sided adhesive tape is strong

572 enough to secure mineral grains, even in vertical scans, but different tapes can vary in terms of

573 clarity and glue thickness.

574   Unknown mineral grains can be picked from a separate and placed directly onto the grain

575 mount with tweezers or a needle. The grains should be placed onto the adhesive tape firmly

576 enough to ensure that enough surface area of the grain is in contact with the tape, but not so

577 firmly that the grain breaks. We recommend strategically distributing the unknown grains in such

578 a way that any individual grain can be easily identified after microCT for further analysis. Grains

579 should be spaced at least one grain length apart to minimize the effect of artifacts from highly

580 attenuation phases. Forming lines or a grid of grains should be avoided since these shapes tend to

581 amplify artifacts. Known mineral standards of expected phases should be included on every grain

582 mount. They can be shards of larger crystals or mineral grains that have been identified by an

583 independent method, such as through micro-Raman spectroscopy. These standard grains should

584 broadly match the grain sizes of the unknowns and be distributed throughout the grain mount in

585 the same way as the unknowns to account for any spatial variation in X-ray attenuation. In some

586 cases, the mineral standard can also be used as the age standard for further analysis (e.g.,

587 Durango apatite).

588   Vertical grain mount scans produce overall better results by reducing microCT artifacts

589 (see Fig. 7). However, horizontal scans are likely sufficient in many applications, such as

590 distinguishing apatite and zircon, and allow multiple grain mounts to be stacked on top of the

591 sample holder. This allows 4-times the number of grains in a single scan (up to 400 grains). The

592 resulting file sizes will be bigger, but the scan time is the same.

593   Scan time will vary based on the instrument. Here we show that for simple mineral

594 identification, rapidly acquired (< 20 min on the Rigaku CT LABHX) microCT data can be used

595 to visually identify zircon from apatite or other phases. This can be done with little technical

596 training by inspecting reconstructed grayscale photo slices using freely available software such

597 as ImageJ (Schneider et al., 2012). For a more quantitative record or if the separation of phases

598 with a small, weak density contrast (such as apatite and titanite) is required, grains can be

599 segmented with more specialized software (such as Dragonfly), and average grayscale values can

600 be extracted for each grain.

601   For some geo- and thermochronology applications it is necessary to detect inclusions or

602 fractures and measure grain volume and surface area. For these applications, in addition to

603 mineral verification, we recommend longer scan times (~2 h with the Rigaku CT LABHX),

604 which yields a better spatial resolution. These data can be processed the same way as described

605 above using, for example, ImageJ or Dragonfly, to yield grain-specific 3D volume and surface

606 area measurements used to calculate F_T and/or grain mass in (U-Th)/He thermochronology.

607 Users may also use Blob3D (Ketcham, 2005), a free software package to directly calculate 3D F_T

608 correction factors.

3.6 Benefits of microCT in geo- and thermochronology

610   Here we present a rapid method for identifying or verifying apatite and/or zircon crystals

611 in separates using microCT as a screening technique. This can serve several purposes depending

612 on the goal of the research. First, it can reduce the misidentification of minerals prior to costly

613 and time-intensive analyses. In the case of precious or low-yield samples, reducing human error

614 is especially important.

615   The 3D grain-specific measurements acquired during the micro-CT scan provide added

616 value to (U-Th)/He thermochronology research where grain shapes are used to calculate Ft

617 corrections and directly impact age calculations. These corrections typically assume a mineral

618 grain geometry and use a set of 2D microscope measurements by a lab member defining

619 dimensions across a crystal using a computer image (e.g., Farley et al., 1996; Gautheron et al.,

620 2021). The exact procedure for measuring individual crystals varies by laboratory (e.g., assumed

621 grain geometries, number of 2D measurements made). Recent work has used microCT to

622 calculate 3D Ft and/or validate 2D Ft measurements (Evans et al., 2008; Glotzbach et al., 2019;

623 Cooperdock et al., 2019). The method presented here yields data that can be directly used with

624 the Blob3D software for 3D Ft calculation, or provide more precise grain-specific surface area

625 and volume measurements for calculating Ft by hand.

626   For detrital geochronology, the microCT pre-screening method described here can be

627 used to identify mineral phases regardless of grain geometry, thereby enabling the use of grains

628 with less-than-ideal geometries. Since apatite and zircon are mainly picked under a binocular

629 microscope based on their grain shape, sub-euhedral or broken crystals, which typically represent

630 the bulk of the crystals in a given separate, are often not chosen for further analysis. This can

631 present a problem for samples with low yields or bias the results to grains of specific

632 morphologies (i.e., histories or age populations).

633   Furthermore, this method can be expanded beyond apatite, zircon, and titanite. For

634   example, we did not analyze monazite or rutile in this study. However, based on the MuCalc

635   modeling and the characteristics of the microCT scans analyzed here, monazite and rutile should

636   be distinguishable from apatite, zircon, and titanite at X-ray energies below ~200 keV, with a

637   greater distinction between these phases at lower X-ray energies. The separation of common

638   detrital minerals, such as apatite, zircon, titanite, monazite, and rutile in a grain mount, crushate,

639   or rock sample could also be used for detrital heavy mineral analysis.

640   In laboratories with ready access to a microCT instrument, this protocol can be

641   incorporated into the primary workflow for (U-Th)/He analysis and reduce the amount of time

642   spent at the picking microscope. Apatite and zircon grains can be placed directly onto a microCT

643   mount without the need for careful identification or 2D measurements. A 2-hour microCT scan

644   would provide mineral ID verification, screen for inclusions or fractures, and provide 3D grain

645   specific volume and surface area measurements. Once data reduction and processing protocols

646   are established and users are trained, data analysis can take anywhere from 15 minutes to a few

647   hours depending on the size of the dataset. More than 100 grains (including known mineral

648   standards) can be placed onto a single mount and scanned vertically, or multiple mounts can be

649   stacked horizontally allowing for several hundred grains to be scanned and analyzed in a single

650   session.

651   If microCT access is less available, the protocol may be used for particularly difficult to

652   identify, precious, or low-yield samples. This technique can also be used for detrital zircon

653   studies (U-Pb or (U-Th)/He) to reduce sampling bias toward more morphologically perfect

654   crystals by pre-screening a large number of grains and using microCT to identify zircon grains

655   for further analysis based on their density rather than grain shape.

656   **4 Conclusions**

657   We show that microCT pre-screening of grains picked from separates can be used to

658   unequivocally distinguish apatite and zircon, and to distinguish apatite and zircon from other

659   phases, such as titanite, with a degree of certainty. Normalizing grayscale values of grains from

660   microCT volumes by the average value of a known zircon standard accounted for differences in

661   experimental setup, instrument performance, and processing from one mount to the next. The

662   remaining observed variation of grayscale values within and between grains is likely due to

663   grain-specific natural variability of material parameters, such as crystal damage and elemental

664   substitution.

665   We recommend the following best practices for future studies:

666   ● Mineral standards for normalization should be matched in size to the unknown samples to
667   account for the effect of beam hardening.

668   ● Standards should be distributed throughout the mount, and sample grains should be
669   normalized by the closest standard grain to minimize minor spatial effects.

670   ● The mount should be tilted vertically for the microCT data acquisition to reduce the
671   effect of shadowing from neighboring grains. MicroCT instrument geometries other than
672   the one used here might require different mount orientations.

673   ● For the particular microCT instrument used here, the signal-to-noise ratio did not
674   improve significantly past 17 min for continuous scans. A step scan of about 2 h (50 min
675   counting time) was sufficient to produce high-resolution data with a usable signal-to-
676   noise ratio.

677   MicroCT scans that are set up according to the recommendations are a robust method to

678   distinguish between apatite and zircon in mounts of selected grains. This offers a possible

679   alternative to separating apatite from zircon using highly-toxic MEI. Grains can be picked

680   directly from separates that have undergone a density separation with non-toxic LST, LMT, or

681   SPT, which is a less laborious and safer process. As an additional benefit, the data acquired in

682   this process can also be used to screen the sample grains for fluid and mineral inclusions and to

683   model alpha-ejection and -implantation corrections for (U-Th)/He dating (Evans et al., 2008;

684   Cooperdock et al., 2019).

685   **Data availability**

686   Reconstructed microCT volumes for all mounts, X-ray energies, and scan times are stored at the

687   USCHelium Lab and are available on request.

688   **Author contribution**

689   EHGC and FH conceptualized the study and experimental design with input from AT; AC

690   collected FCT samples; FH, RMC, and AC prepared samples and collected data; all co-authors

691 contributed to data interpretation; FH and RMC prepared figures; EHGC and FH prepared and
692 edited the manuscript draft with input from RMC, AC, AT, and AJC.

693 **Competing interests**

696 **Acknowledgments**

705 **Financial support**

709 **References**

710 Alves, H., Lima, I., and Lopes, R. T.: Methodology for attainment of density and effective
711   atomic number through dual energy technique using microtomographic images, Appl.
712   Radiat. Isot., 89, 6-12, https://doi.org/10.1016/j.apradiso.2014.01.018, 2014.
713 Buijs, W., Van Der Gen, A., Mohn, G. R., and Breimer, D. D.: The direct mutagenic activity of
714   α, ω-dihalogenoalkanes in Salmonella typhimurium: Strong correlation between
715   chemical properties and mutagenic activity, Mutat. Res. Lett., 141(1), 11-14,
716   https://doi.org/10.1016/0165-7992(84)90029-0, 1984.

717 Bowring, S. A., and Schmitz, M. D.: High-precision U-Pb zircon geochronology and the
718   stratigraphic record, Rev. Mineral. Geochem., 53, 305-326,
719   https://doi.org/10.2113/0530305, 2003.

720 Cooperdock, E. H., Ketcham, R. A., and Stockli, D. F.: Resolving the effects of 2-D
721   versus 3-D grain measurements on apatite (U–Th)/ He age data and reproducibility,
722   GChron, 1, 17-41, https://doi.org/10.5194/gchron-1-17-2019, 2019.

723 Dragonfly 2021.1 [Computer software]. Object Research Systems (ORS) Inc, Montreal, Canada,
724   2021; http://www.theobjects.com/dragonfly.

725 Donelick, R. A., O'Sullivan, P. B., and Ketcham, R. A. (2005). Apatite fission-track analysis.
726   Reviews in Mineralogy and Geochemistry, 58, 49-94,
727   https://doi.org/10.2138/rmg.2005.58.3, 2005.

728 Dumitru, T. A., and Stockli, D. F.: A better way to separate apatite from zircon using
729   constriction tubes, Advances in Fission-Track Geochronology, 10, 325-330, 1998.

730 Evans, N. J., McInnes, B. I., Squelch, A. P., Austin, P. J., McDonald, B. J., and Wu, Q.:
731   Application of X-ray micro-computed tomography in (U–Th)/He thermochronology,
732   Chem. Geol., 257, 101-113, https://doi.org/10.1016/j.chemgeo.2008.08.021, 2008.

733 Farley, K. A.: (U-Th)/He Dating: Techniques, Calibrations, and Applications, Reviews in
734   Mineralogy and Geochemistry, 47, 819-844, https://doi.org/10.2138/rmg.2002.47.18,
735   2002.

736 Farley, K. A., Wolf, R. A., and Silver, L. T.: The effects of long alpha-stopping distances on
737   (U-Th)/He ages, Geochim. Cosmochim. Acta, 60(21), 4223-4229,
738   https://doi.org/10.1016/S0016-7037(96)00193-7, 1996.

739 Farley, K. A., Treffkorn, J., and Hamilton, D.: Isobar-free neon isotope measurements of flux-
740   fused potential reference minerals on a Helix-MC-Plus10K mass spectrometer, Chem.
741   Geol., 537, 119487, https://doi.org/10.1016/j.chemgeo.2020.119487, 2020.

742 Gautheron, C., Pinna-Jamme, R., Derycke, A., Ahadi, F., Sanchez, C., Haurine, F.,
743   Monvoisin, G., Barbosa, D., Delpech, G., Maltese, J., Sarda, P., and Tassan-Got, L.:
744   Analytical protocols and performance for apatite and zircon (U–Th)/ He analysis on
745   quadrupole and magnetic sector mass spectrometer systems between 2007 and 2020,
746   GChron, 3, 351-370, https://doi.org/10.5194/gchron-3-351-2021, 2021.

747 Glotzbach, C., Lang, K. A., Avdievitch, N. N., and Ehlers, T. A.: Increasing the accuracy of (U-

748 Th(-Sm))/He dating with 3D grain modelling, Chem. Geol., 506, 113–125,

749 https://doi.org/10.1016/j.chemgeo.2018.12.032, 2019.

750 Guenthner, W. R., Reiners, P. W., and Chowdhury, U.: Isotope dilution analysis of Ca and Zr in

751 apatite and zircon (U-Th)/He chronometry, Geochem., Geophys., Geosyst., 17, 1623-

752 1640, https://doi.org/10.1002/2016GC006311, 2016.

753 Hauff, P. L., and Airey, J.: The handling, hazards, and maintenance of heavy liquids in the

754 geologic laboratory, USGS Circular 827, https://doi.org/10.3133/cir827, 1980.

755 Hanna, R. D., and Ketcham, R. A.: X-ray computed tomography of planetary materials: A primer

756 and review of recent studies, Geochem., 77, 547-572,

757 https://doi.org/10.1016/j.chemer.2017.01.006, 2017.

758 Holland, H. D., & Gottfried, D.: The effect of nuclear radiation on the structure of zircon, Acta

759 Crystallogr., 8, 291-300, https://doi.org/10.1107/S0365110X55000947, 1955.

760 Hughes, J. M., Cameron, M., & Crowley, K. D.: Structural variations in natural F, OH, and Cl

761 apatites, Am. Mineral., 74, 870-876, 1989.

762 Ketcham, R. A., and Carlson, W. D.: Acquisition, optimization and interpretation of X-ray

763 computed tomographic imagery: applications to the geosciences, Comput. Geosci., 27,

764 381-400, https://doi.org/10.1016/S0098-3004(00)00116-3, 2001.

765 Ketcham, R. A.: Computational methods for quantitative analysis of three-dimensional features

766 in geological specimens, Geosphere, 1, 32-41, 2005.

767 Koroznikova, L., Klutke, C., McKnight, S., and Hall, S.: The use of low-toxic heavy suspensions

768 in mineral sands evaluation and zircon fractionation, J. South. Afr. Inst. Min. Metall.,

769 108, 25-33, 2008.

770 Lafuente, B., Downs, R. T., Yang, H., and Stone, N.: The power of databases: the RRUFF

771 project, in: Highlights in Mineralogical Crystallography, edited by: Armbruster, T., and

772 Danisik, R. M., W. De Gruyter, Berlin, Germany, 1-30,

773 https://doi.org/10.1515/9783110417104-003, 2015.

774 Lippolt, H. J., Leitz, M., Wernicke, R. S., and Hagedorn, B.: (Uranium + thorium)/helium dating

775 of apatite: experience with samples from different geochemical environments, Chem.

776 Geol., 112, 179-191, https://doi.org/10.1016/0009-2541(94)90113-9, 1994.

777 McDowell, F. W., McIntosh, W. C., and Farley, K. A.: A precise ^{40}Ar–^{39}Ar reference age for the

778   Durango apatite (U–Th)/He and fission-track dating standard. Chem. Geol., 214, 249-

779   263, https://doi.org/10.1016/j.chemgeo.2004.10.002, 2005.

780   Mounteney, I.: The use of lithium heteropolytungstate as an alternative to bromoform for heavy

781   media separations, British Geological Survey IR/11/049, Nottingham, UK, 1-20,

782   http://nora.nerc.ac.uk/id/eprint/519459, 2011.

783   Munsterman, D., and Kerstholt, S.: Sodium polytungstate, a new non-toxic alternative to

784   bromoform in heavy liquid separation, Review of Palaeobotany and Palynology, 91, 417-

785   422, https://doi.org/10.1016/0034-6667(95)00093-3, 1996.

786   Osterman-Golkar, S., Hussain, S., Walles, S., Anderstam, B., and Sigvardsson, K.: Chemical

787   reactivity and mutagenicity of some dihalomethanes, Chem.-Biol. Interact., 46, 121-130,

788   https://doi.org/10.1016/0009-2797(83)90011-x, 1983.

789   Roldán-Arjona, T., and Pueyo, C.: Mutagenic and lethal effects of halogenated methanes in the

790   Ara test of Salmonella typhimurium: quantitative relationship with chemical reactivity,

791   Mutagenesis, 8, 127-131, https://doi.org/10.1093/mutage/8.2.127, 1993.

792   Schneider, C. A., Rasband, W. S., and Eliceiri, K. W.: NIH Image to ImageJ: 25 years of image

793   analysis, Nature methods, 9, 671-675, https://doi.org/10.1038/nmeth.2089, 2012.

794   Tagami, T., and O'Sullivan, P. B.: Fundamentals of fission-track thermochronology, Rev.

795   Mineral. Geochem., 58, 19-47, https://doi.org/10.2138/rmg.2005.58.2, 2005.

796   Van Bladeren, P. J., Breimer, D. D., Rotteveel-Smijs, G. M. T., and Mohn, G. R.: Mutagenic

797   activation of dibromomethane and diiodomethane by mammalian microsomes and

798   glutathione S-transferases, Mutat. Res., Environ. Mutagen. Relat. Subj., 74, 341-346,

799   https://doi.org/10.1016/0165-1161(80)90192-2, 1980.

800   Vance, E. R., and Metson, J. B.: Radiation damage in natural titanites, Phys. Chem. Miner., 12,

801   255-260, https://doi.org/10.1007/BF00310337, 1985.

802   Vermeesch, P., Seward, D., Latkoczy, C., Wipf, M., Günther, D., and Baur, H.: α-Emitting

803   mineral inclusions in apatite, their effect on (U–Th)/He ages, and how to reduce it,

804   Geochim. Cosmochim. Acta, 71, 1737-1746, http://dx.doi.org/10.1016/j.gca.2006.09.020,

805   2007.

806   Weimerskirch, P. J., Burkhart, K. K., Bono, M. J., Finch, A. B., and Montes, J. E.: Methylene

807   iodide poisoning, Annals of emergency medicine, 19, 1171-1176,

808   https://doi.org/10.1016/S0196-6644(05)81524-0, 1990.

809